ACS APPLIED ENGINEERING MATERIALS

pubs.acs.org/acsaenm Article

Graphitized Mesoporous Engineered Carbon Support for Fuel Cell Applications

Nagappan Ramaswamy,* Barr Zulevi, Geoff McCool, Zixiao Shi, Aldo Chavez, David A. Muller, Anusorn Kongkanand, and Swami Kumaraguru

Cite This: *ACS Appl. Eng. Mater.* 2023, 1, 2543−2554

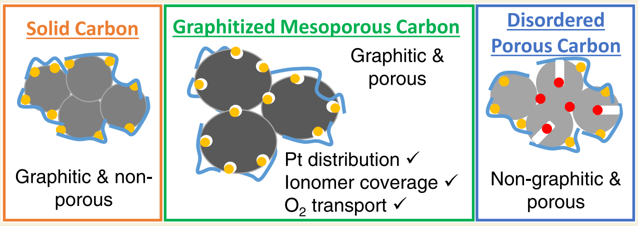

ABSTRACT: As proton exchange membrane fuel cells mature into commercial devices capable of powering a wide range of stationary and automotive applications, they need materials with tunable properties to improve their performance and durability. Carbon supports used for platinum (Pt) nanoparticle dispersion is typically based on a furnace black-type material with a random structure, thereby hindering progress in catalyst development. To address this challenge, engineered carbons with a tunable mesoporous structure offer an opportunity to maximize catalyst performance and durability. In this article, we report on the development of a graphitized, mesoporous carbon support with a high degree of ordering, labeled here as ECS4005, for the dispersion of Pt nanoparticles. Pt/ECS4005 shows significantly improved kinetic activity due to its mesoporous structure that mitigates Pt poisoning by sulfonate functional groups in the ionomer while simultaneously enabling favorable accessibility to reactants.

KEYWORDS: *engineered carbon support, graphitized mesoporous, fuel cell cathode, Pt/ECS4005, catalyst coarsening*

1. INTRODUCTION

Proton exchange membrane fuel cells (PEMFC) are on the verge of widespread commercialization for powering heavy-duty truck vehicles and displacing the emission-intensive diesel-based internal combustion engines. PEMFCs have a combination of favorable characteristics such as high energy conversion efficiency, fast refueling, high torque, low noise, and environmentally friendly when green hydrogen is utilized.[1] The United States Department of Energy (DOE) has established an ultimate heavy-duty vehicle performance and durability combined target of 2.5 kW/g_{Pt} after 30,000 h equivalent of operation with a total membrane electrode assembly (MEA) Pt loading of ≤ 0.25 mg_{Pt}/cm^2 for Class 8 long-haul tractor-trailers. Ultimate cost and peak efficiency targets are 60 \$/kW and 72%.[2] Durability or stack lifetime becomes very crucial as the cost of hydrogen fuel gets amortized over the 30,000 h of operation to decrease the total cost of ownership (TCO) of the fuel cells.

As fuel cell technology becomes more mature, active materials with tunable properties become necessary to meet demanding performance and durability targets. Pt and Pt-alloy nanoparticles currently remain the only viable commercial option for use as anode and cathode catalysts.[3−5] The nature of these catalyst materials is strongly dependent on the nature of the carbon support upon which they are dispersed.[6−8] Carbon materials used as catalyst supports range from furnace black materials,[9−11] one-dimensional (1D) nanomaterials such as carbon nanotubes (CNT),[12] graphene,[13,14] ordered mesoporous materials,[15,16] and engineered materials[17,18] designed bottom-up using organic precursors. 1D nanomaterials, such as single-walled and multiwalled CNTs, are widely studied due to their favorable carbon corrosion properties, but they remain fairly expensive and not usually available in high purity.[19] Graphene has also been widely studied due to its high surface area and tunable surface chemistry, but it is usually very hydrophilic and leads to rapid degradation of Pt nanoparticles due to poor anchoring on the carbon support.[20] Ordered mesoporous carbon supports are effective model systems due to their open mesopores but are very expensive and not available in smaller particle sizes for commercial applications.[15,16] A MgO-templated mesoporous carbon, labeled CNovel, was developed for the dispersion of Pt nanoparticles inside the mesopore structure that demonstrated improved performance by mitigating poisoning by ionomer functional groups.[17] Several recent studies have developed nitrogen functionalization of either a bottom-up designed carbon support from organic precursors[21] or commercially available

Received: June 27, 2023
Revised: September 27, 2023
Accepted: September 28, 2023
Published: October 12, 2023

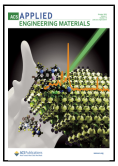

https://doi.org/10.1021/acsaenm.3c00354

furnace blacks[22−24] to either improve Pt anchoring or improve ionomer distribution on the catalyst surface.

Furnace blacks such as KetjenBlack, Vulcan XC-72R, and Acetylene Black are well-studied carbon materials for the dispersion of Pt/Pt-alloy nanoparticles. Available in a range of surface areas from 200 to 1500 m^2/g, they also offer a range of graphitization levels as measured by Raman disorder/graphitization (D/G) peak ratios.[8,11] KetjenBlack EC-300-J is a particularly well-known high surface area carbon (HSC) material that is microporous with a large internal surface area, as well as turbostatic, disordered, and nongraphitized.[9] Pt nanoparticles are dispersed on the internal surface area of the carbon, thereby preventing Pt from direct poisoning by a perfluoro sulfonic acid (PFSA) ionomer used in the fuel cell electrode for proton transport functionality and resulting in enhanced kinetic properties.[9,10] Further, due to the presence of micro/mesopores, deposited Pt nanoparticles are observed to be more durable as these pores and surface defects tend to anchor the Pt more strongly and hence prevent coalescence.[25] However, these carbon supports suffer from large proton transport losses and local-O_2 transport losses due to their large macroporous and microporous surface area, leading to poor catalyst accessibility.[9] On the other hand, Vulcan-type medium surface area carbon (MSC), with solid primary particles and a more ordered carbon surface with less functional group concentration, hosts most of the Pt on the external surface, which leads to poor kinetic performance and poor durability due to enhanced agglomeration of the nanoparticles. However, MSCs do feature better reactant accessibility with lower proton transport and local-O_2 transport resistances, given their low micro- and macroporosity.[9] It would be desirable to combine the favorable properties of HSC and MSC supports with accessible mesopores such that the Pt nanoparticles are located away from the ionomer for better kinetic performance while simultaneously being strongly bound with the carbon support to maintain improved durability.

In this article, we describe and demonstrate a novel engineered catalyst support (ECS) developed by Pajarito Powder, LLC, with a desired combination of characteristics, including higher mesoporosity for Pt dispersion, an open hierarchical pore structure for improved reactant (H^+/O_2) accessibility, improved kinetic activities due to mitigated ionomer poisoning and overall better performance in fuel cell MEAs.[18] This carbon support is referred to throughout as ECS4005 and achieved better initial performance due to the improved accessibility and mitigated ionomer poisoning. To increase the durability of the carbon support, it was heat treated at a higher temperature, leading to the formation of well-ordered, graphitic crystal planes. The electrochemical and physical properties of Pt/ECS4005 are compared to those of commercially available Pt/HSC and Pt/MSC catalysts. The Pt/ECS4005 catalyst represents a significant improvement over a conventional solid carbon such as Pt/MSC, and the results are discussed here in detail.

2. EXPERIMENTAL SECTION

2.1. Catalysts Materials and MEA Fabrication

ECS4005, a commercially available carbon support, was produced by Pajarito Powder using their VariPore technology. The general ECS production method has been described in refs 26−30. A simple description of the process is that a mixture of a metal precursor, nitrogen-rich organic precursor, and fumed silica is pyrolyzed. Afterward, the silica template is removed by a hydrofluoric acid treatment. The carbon is then washed, dried, and heat treated under a controlled atmosphere. After a few more proprietary processing steps, the ECS4005 carbon support is then platinized, resulting in Pt/ECS4005 with a nominal 30 wt % Pt. Pt supported on a KetjenBlack EC-300J (HSC) and Vulcan XC-72R (MSC) at a nominal loading of 30% was procured from a commercial supplier. Cathode catalyst inks were made by dispersing the catalyst in an *n*-propanol to water (3:1) solvent mixture with a PFSA ionomer featuring medium side chain length and an equivalent weight of 825 g/mol. Optimized ionomer-to-carbon ratios of 0.90, 0.75, and 0.80 were used for Pt/HSC, Pt/MSC, and Pt/ECS4005, respectively. Cathode inks were coated on decal substrates at 0.10 mg_{Pt}/cm^2. All anode catalyst layers were composed of a 10% Pt/C catalyst at a fixed loading of 0.025 mg_{Pt}/cm^2 and an ionomer-to-carbon ratio of 0.6. MEAs with a 5 cm^2 active area were fabricated via decal transfer of the anode and cathode catalyst layers on either side of a 12 μm thick, 800EW PFSA membrane in the H^+ form. A roughly 230 μm thick carbon fiber paper-based gas diffusion layer was used on both the anode and cathode side.

2.2. Physical Characterizations of Catalysts

Analysis of the N_2-adsorption surface area and pore size distribution of the catalyst powders was carried out using a Micromeritics Instrument Corporation ASAP 2020 Physisorption system. N_2 gas of ultrahigh purity was used, and the measurements were conducted at 77 K. The total specific surface area of the catalyst was determined using the Brunauer−Emmett−Teller (BET) procedure in the range of 0.05−0.2 N_2 partial pressure, pore size distribution was quantified using Barrett−Joyner−Halenda (BJH) methodologies, and the micropore surface area was quantified using the t-plot analysis. Water uptake was measured volumetrically with a 3Flex Dynamic Vapor Sorption instrument at 25 °C. Characterization of the crystal structures and graphitic nature of the samples was performed by using X-ray diffraction (XRD) on a Rigaku MiniFlex 600 (Rigaku Co., Japan) with monochromated Cu Kα radiation (λ = 1.5406 Å). Raman Spectroscopy was carried out using a Thermo DXR2 Raman spectrometer equipped with a 532 nm laser. Thermogravimetric analysis (TGA) experiments were conducted using a Netzsch STA 449 F1 Jupiter Simultaneous TGA/DSC Thermal Analyzer system. Measurements were conducted using ∼10 mg of the sample in an air flow of 10 mL/min at a rate of 10 °C/min from 20 to 800 °C.

2.3. Electrochemical Diagnostics and Characterizations

In situ characterizations of the MEA to quantify various cathode properties such as kinetic activity, H-adsorption electrochemically active surface area (ECSA), CO adsorption/stripping ECSA, H_2/air polarization curves, and H^+ and O_2 transport resistances were carried out in a single-cell test fixture comprising 5 cm^2 active area MEA (0.5 mm lands/channels). Prior to performance and durability measurements, MEAs were subjected to an extensive ∼30 h break-in protocol that involved activation cycles and voltage recovery steps. The details of the break-in protocol are available elsewhere.[31] ECSA was quantified via integration of the hydrogen adsorption/desorption (H_{UPD}) region from cyclic voltammetry measurements of the cathode carried out at room temperature and 100% relative humidity (RH) conditions using H_2 and N_2 gas feeds on the anode and cathode sides at flow rates of 0.2/0.2 slpm, respectively. Oxygen reduction reaction (ORR) activities were measured at 0.9 V using the polarization curves obtained with pure H_2 and O_2 as the reactant gases in the anode and cathode, respectively, at a stoic of 20. The RH of the inlet gas was maintained at 100%, with the cell temperature maintained at 80 °C at an absolute outlet pressure of 150 kPa_{abs}. The activity at 0.9 V was determined using the Tafel plot, which is a semilog plot of the Ohmic-resistance-corrected cell voltage versus H_2 gas crossover corrected current density. H_2/air polarization curves with a high stoichiometric feed of the reactant gases were measured at various operating conditions with cell temperatures ranging from 80 to 94 °C, RH values from 65 to 100%, and absolute outlet pressures of 150−250 kPa_{abs}. High-frequency resistance (HFR) to quantify the sum of cell electronic resistance and membrane H^+ transport resistance was measured at an alternating current (AC) frequency of 5 kHz.

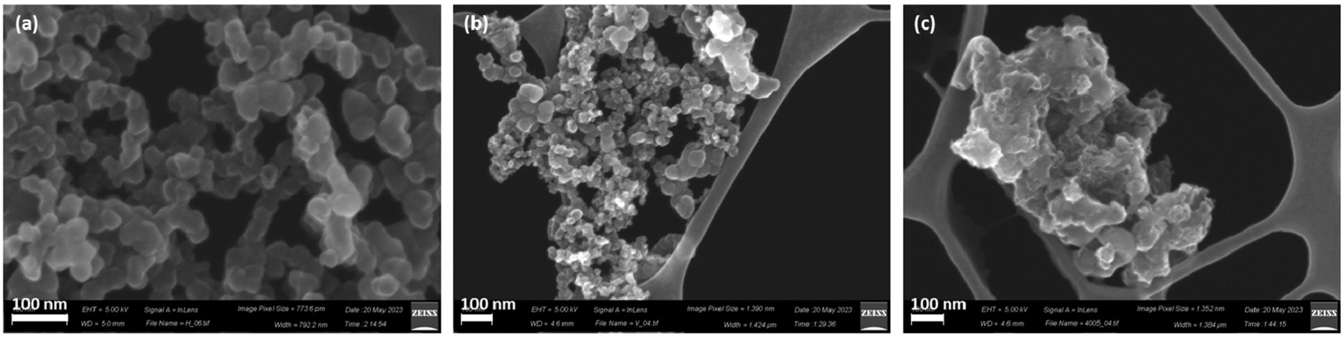

Figure 1. Representative SEM images of the (a) HSC, (b) MSC, and (c) ECS4005 carbon support materials.

A cathode catalyst-specific accelerated stress test (AST) recommended by the U.S. DOE was used in this study, which consisted of 30,000 trapezoidal voltage cycles from 0.6 to 0.95 V. The dwell time at each voltage was 2.5 s, and the ramp time was 0.5 s. Each cycle takes 6 s. AST durability protocols were carried out in 5 cm^2 MEAs with H_2/N_2 flow at 80 °C, 100% RH, and ambient pressure.[32]

Proton transport resistance of the catalyst layer was measured using an electrochemical impedance spectra (EIS) methodology,[33] which involved the flow of H_2 on the anode and N_2 on the cathode at 80 °C and various RH values from 20−122%. EIS measurement was conducted to quantify proton conduction resistance at a DC potential of 0.2 V with 0.15 mV amplitude from a frequency of 0.5 Hz to 20 kHz with 20 points per decade. The EIS profile was fitted to a transmission line model from which the proton transport resistance in the membrane ($R_{\mathrm{H+,membrane}}$) and the cathode catalyst layer ($R_{\mathrm{H+,cathode}}$) were obtained. O_2 transport resistance was calculated using the limiting current density measurements at low O_2 partial pressures under operating conditions of 80 °C and 62% RH under differential cell conditions (1 slpm of H_2 and 5 slpm of O_2/N_2 mixtures).[34] O_2 limiting current densities were measured at potentials below 0.3 V at various O_2 mole fractions (1−4%) as a function of outlet pressures (110−300 kPa_{abs}).

2.4. Electron Microscopy

The scanning transmission electron microscopy (STEM) experiment was performed using Thermo-Fisher Titan Themis Cryo S/TEM with a Field Emission Gun (X-FEG), monochromator, and a probe corrector operated at 120 kV and room temperature. The high-annular angle dark field (HAADF) and bright-field (BF) images were collected with 195 mm camera length and 21.4 mrad. convergence angle. The HAADF images were taken with 2048 × 2048 pixels and 2−5 us dwell time. A Zeiss Field Emission Scanning Electron Microscopy (FE-SEM) equipment with an in-lens detector was used to collect images of the carbon support.

3. RESULTS AND DISCUSSION

The physical and chemical properties of the carbon supports were characterized *ex situ* using several techniques to understand their surface characteristics. Representative SEM images of the carbon support are shown in Figure 1. HSC and MSC support materials are represented by an agglomerate of multiple primary particles of an ∼20−30 nm diameter fused together, which are then extensively aggregated to form a connected structure. In contrast, ECS4005 shows a much larger primary particle of ∼0.4−1.0 μm size, which is a result of the templated synthesis process. Surface area and pore size distribution of the ECS4005 carbon support were measured in comparison to the HSC (KetjenBlack) and MSC (Vulcan XC-72R) carbons using N_2 physisorption. The N_2 adsorption isotherms, pore size distribution, along with the micropore profile, are shown in Figure 2, and the surface areas are quantified in Table 1. The N_2 adsorption isotherm of HSC follows the typical type II isotherm in that there is a steep rise indicative of micropores at low partial pressures of $p/p^0 < 0.05$, followed by a characteristic hysteresis at $p/p^0 \sim 0.5{-}0.6$ as well as saturation at $p/p^0 > 0.95$, leading to a rapid uptake in the meso-/macropore region representative of aggregates.[35] The N_2 adsorption isotherm of MSC shows significantly fewer micropores and does not show a major increase until the large meso- and macropore regions. The N_2 adsorption isotherm of ECS4005 also has a subtle micropore region with an increase in N_2 uptake at $p/p^0 > 0.6$, which is a minor indication of ordering in mesopores and a rapid uptake at $p/p^0 > 0.95$ indicative of large aggregates. The total BET and microporous surface areas quantified from the t-plot are shown in Table 1. HSC carbon has a large total surface area of 837 m^2/g with a 152 m^2/g microporous area. Vulcan carbon has a lower total surface area of 241 and an 84 m^2/g microporous area. ECS4005 has a slightly higher total surface area of 351 m^2/g with a lower microporous area of 82 m^2/g.

The adsorption pore size distribution (BJH) shown in Figure 2b clearly delineates the pore structure among the carbon supports. According to the International Union of Pure and Applied Chemistry (IUPAC) definition, regions of adsorption can be classified as micropores (<2 nm), mesopores (2−50 nm), and macropores (>50 nm).[36] HSC has a reasonable micropore and small mesopore contribution inside the primary particles and a macropore contribution greater than 50 nm between the primary particles and aggregates. The MSC material only has a reasonable contribution due to the large mesopores and macropores between primary particles and aggregates. ECS4005 has a more bimodal pore size distribution with a peak dominated at the mesopore ∼10 nm in size and a peak in the 40−80 nm region. These results demonstrate the uniqueness in the pore structure of ECS4005 with a high mesopore fraction at ∼10 nm for Pt nanoparticle dispersion and 40−80 nm for reactant transport. Also shown in Figure 2c is the nonlocal density functional theory (NL-DFT) micropore analysis profile that looks at the pore size distribution in the <2 nm region for the carbon supports. All carbons show a bimodal distribution with peaks at 0.5 and 0.8 nm, with the incremental surface area decreasing in the order HSC > ECS4005 > MSC.

The level of disorder and the degree of graphitization of the carbons were investigated by using Raman spectra and the XRD patterns of the materials. Raman spectra shown in Figure 3a display two peaks at 1300 and 1550 cm^{-1}, commonly known as the disorder (D) and graphitic (G) bands used to evaluate the relative trends in disorder through their ratio of intensities (I_D/I_G).[18] HSC and MSC carbons show disordered content with an I_D/I_G peak ratio of 1.19 for HSC and a lower

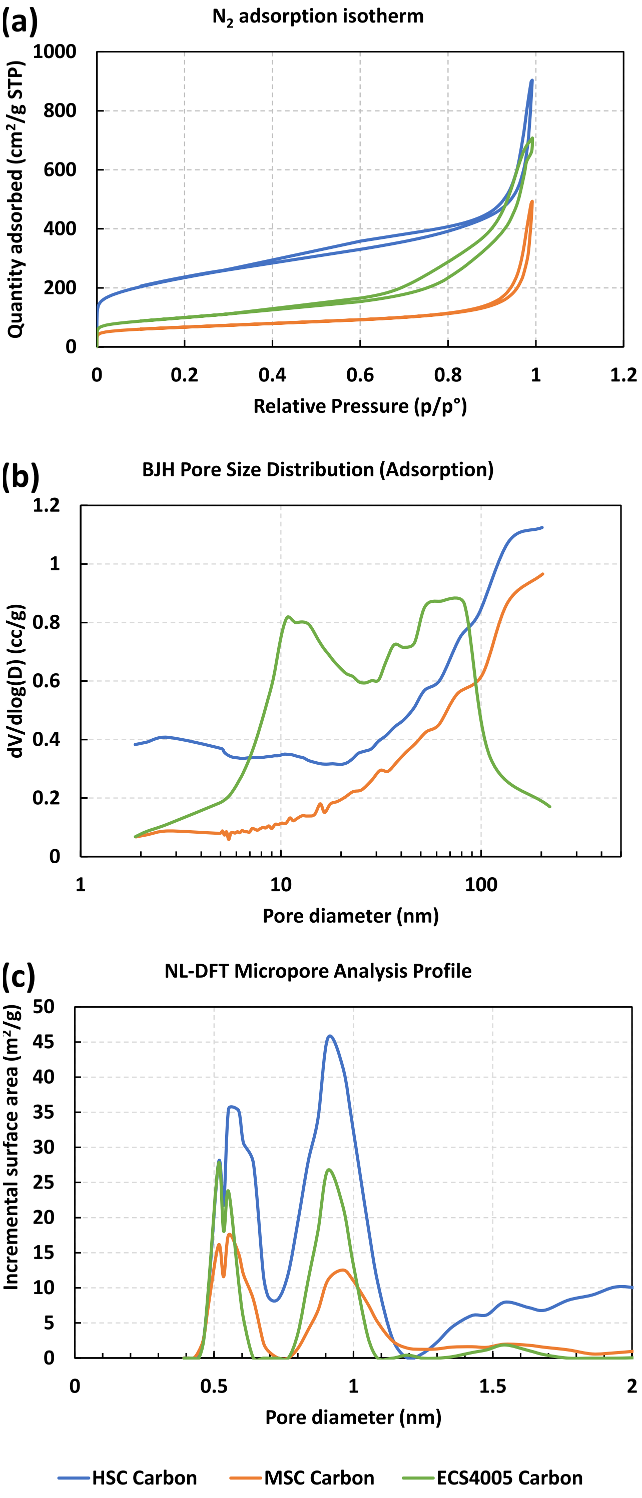

Figure 2. BET-BJH N_2 adsorption measurements of the three carbon supports used in this study showing (a) N_2 adsorption isotherm profile, (b) adsorption pore size distribution (BJH), and (c) micropore analysis profile.

value of 1.03 for MSC carbon. ECS4005 carbon shows much narrower peaks, with the graphitic peak slightly more pronounced and sharper than the disordered peak and an I_D/I_G ratio of 0.95. Further, the appearance of the second-order G' peak at 2680 cm^{-1} confirms the higher degree of graphitic ordering for ECS4005. The carbon crystallite sizes from the inverse of I_D/I_G were calculated according to the equation provided by Cançado et al.[37] and are also reported in Table 1. The larger crystallite size of ECS4005 reflects the higher graphitization levels of the carbon support.

This trend of graphitization in different carbon supports was further confirmed using XRD, as shown in Figure 3b. ECS4005 carbon shows a much more pronounced degree of graphitization as seen by the sharp, well-defined graphitic peak at 2θ of ~23°, which is attributed to the (002) graphitic plane.[18] Further, ECS4005 also shows smaller sharper peaks at 2θ of 42.7, 53.1, and 77°, corresponding to the crystal planes (101), (004), and (110). Contrarily, HSC and MSC materials show only a broader peak at 2θ of 23 and 43°, suggesting that the graphitic planes in these two carbons are of a short-range order and are not crystallized. XRD patterns of Pt/HSC and Pt/ECS4005 are also shown in Figure 3b, which reflects the peaks at 2θ values of 39, 46, 67, and 81° corresponding to the Pt diffraction peaks from (111), (200), (220), and (311), respectively, confirming its face-centered cubic (fcc) structure. The crystallite size of Pt was also calculated from Scherrer's equation from the full width at half-maximum of the Pt (220) diffraction peak and is reported to be 2.5, 2.6, and 2.9 nm for Pt/HSC, Pt/MSC, and Pt/ECS4005 catalysts, respectively.[38] The diffraction peak at a 2θ value of 23° for the graphitic plane of (002) is also seen in the Pt/ECS4005, confirming its presence. Together, Raman spectra and XRD confirm that ECS4005 carbon is much more crystalline and has a higher degree of orderliness in its graphitic structure.

The thermal oxidation stabilities of the three carbon materials and corresponding catalysts are shown in Figure 4. The thermogravimetric profiles were measured as the materials were heated in air at 10 °C/min from 20 to 800 °C. The oxidation of HSC and MSC carbon is initiated at ~590 °C and appears to decompose in a single stage, with MSC as the more stable carbon with a slightly elevated temperature of 720 °C. Despite having a higher level of graphitization observed by XRD and Raman spectroscopy, the thermal oxidation of ECS4005 carbon was initiated earlier than HSC and MSC. Further, the platinized carbon samples show a similar trend with a lower temperature of oxidation. The Pt/ECS4005 catalyst does show a stable plateau at 400 to 480 °C, which then starts to oxidize by 580 °C. The plateau at >600 °C of the catalysts confirms the ash content of the material to be 28.3% for Pt/HSC and 28.7% for Pt/MSC and Pt/ECS4005 by weight. It is hypothesized that a trace amount of metal residues (such as nickel in ppm quantities) leftover from the ECS4005 carbon preparation can catalyze carbon oxidation, resulting in earlier thermal oxidation for ECS4005. This may or may not translate to catalyst durability in a fuel cell as it is governed by an electrochemical reaction.

The volumetric water uptake profile during adsorption at 25 °C from the 3Flex Dynamic Vapor Sorption (DVS) instrument is shown in Figure 5 as a function of the water partial pressure (p/p^0). There is no uptake of water at a low p/p^0 of 0.2 due to hydrophobic carbon planes. Water uptake increases at $p/p^0 >$ 0.24 for all three carbons, possibly due to the oxygen functional groups and the presence of mesopores. An inflection point at $p/p^0 > 0.55$ is observed for HSC carbon due to the adsorption of water molecules in the micropores, the absence of which for MSC and ECS4005 materials confirm the lack of micropores.[39] The water uptake reported here was measured as a way to diagnose the surface properties of the carbon support powder only. This does not necessarily reflect the catalyst layer since the ionomer content will affect the water uptake as well.

Table 1. Physical Properties of the Carbon Support and the Catalyst Materials

catalyst	Pt metal loading (%)	surface area (m^2/g_{Carbon}) total BET	surface area (m^2/g_{Carbon}) micropores	Raman I_D/I_G ratio	carbon crystallite size, L_a (nm)	Pt XRD particle size (nm)
HSC	28.3	837	152	1.19	16.2	2.5
Vulcan	28.7	241	84	1.03	18.7	2.6
ECS4005	28.7	351	82	0.95	20.2	2.9

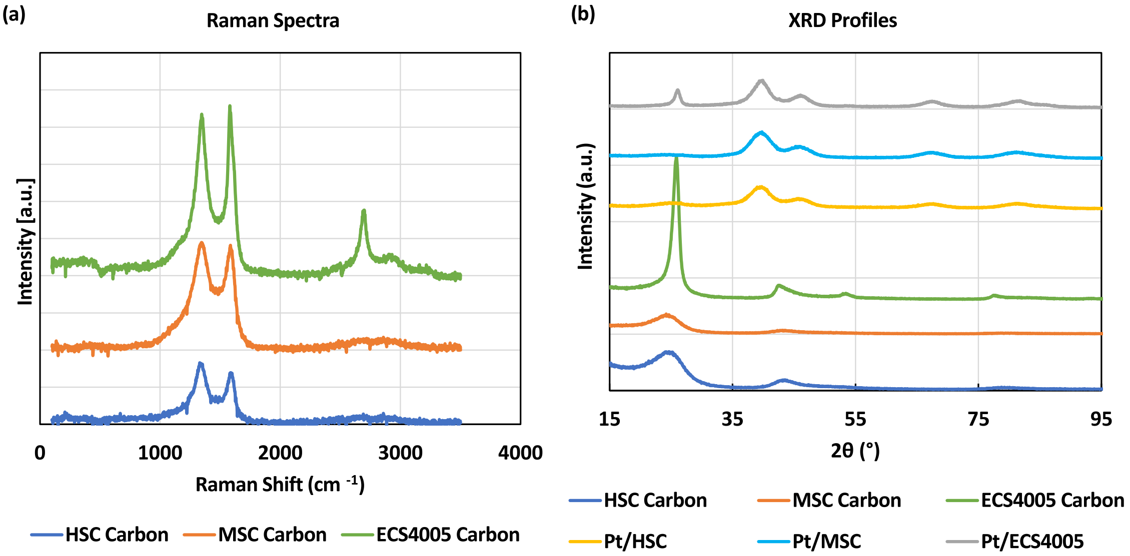

Figure 3. (a) Raman spectra and (b) X-ray diffraction profiles of the carbon supports.

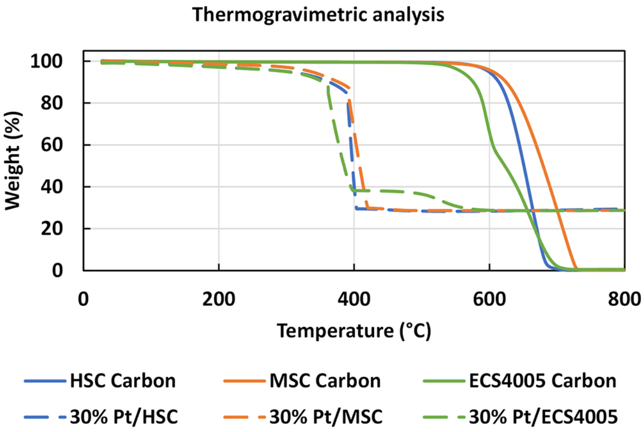

Figure 4. Thermogravimetric profiles of the carbon supports and catalyst materials. Materials were heat treated in air flow at 10 °C/min.

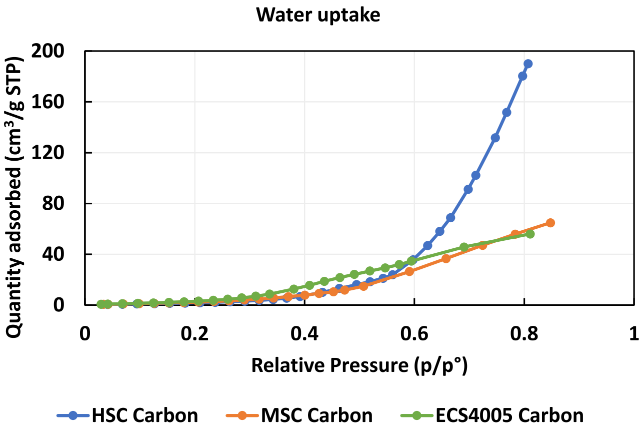

Figure 5. Volumetric water uptake of the carbon supports was measured in a 3Flex Dynamic Vapor Sorption system at 25 °C.

Figure 6 shows the ECSA measured from hydrogen underpotential deposition (H_{UPD}), cathode double-layer capacitance (C_{DL}), mass activity, and specific activity of the three catalysts at the beginning of life (BOL) and at the end of the test (EOT) after a cathode catalyst-specific AST comprising 80 °C, H_2/N_2, 104 kPa_{abs}, and 0.60 to 0.95 V for 30,000 cycles. Cathode ECSA is slightly higher at 75 m^2/g for Pt/HSC catalysts at BOL due to the large surface area of the carbon and better dispersion of Pt compared to slightly smaller values of 54 and 62 m^2/g for Pt/MSC and Pt/ECS4005 catalysts, respectively. It degrades to 25 m^2/g for Pt/ECS4005 at EOT, which is intermediate between that of Pt/HSC (~33 m^2/g) and Pt/MSC (10 m^2/g) catalysts. HSC is microporous and anchors and disperses Pt better, whereas the MSC and ECS4005 carbons are more graphitic and lead to more coalescence of the Pt nanoparticles.[8,25,40] Hence, Pt/HSC has a higher ECSA compared to moderately lower values for Pt/MSC and Pt/ECS4005. Pt/HSC has a higher surface area and shows a higher C_{DL} at BOL of 46 mF/cm^2 compared to 41 and 38 mF/cm^2 for Pt/MSC and Pt/ECS4005. They degrade to roughly 40 mF/cm^2 for Pt/HSC and 28−29 mF/cm^2 for the Pt/MSC and Pt/ECS4005 catalysts. C_{DL} is the sum of the capacitances from Pt and the carbon interface with water and the ionomer.[41] Given that the carbon does not corrode significantly in the catalyst-specific AST conducted, the loss in C_{DL} corresponds to the loss of the Pt interface with ionomer/water in the catalyst layer.

Figure 6c,d shows the kinetic activities, and Figure 7 shows the H_2/O_2 polarization curves in the kinetic current density

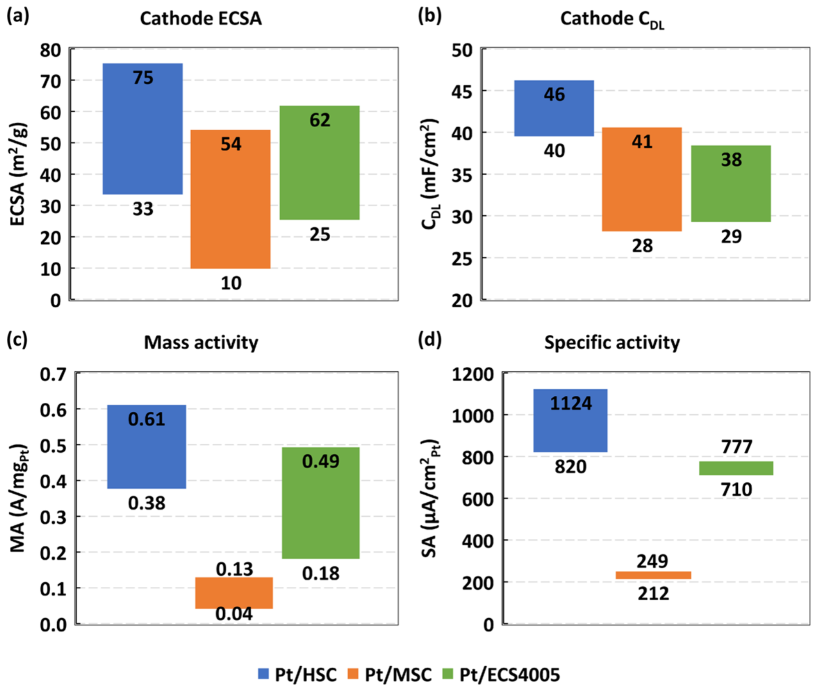

Figure 6. Electrochemical characterizations of the catalysts: (a) ECSA, (b) double-layer capacitance, (c) Pt-mass activity, and (d) Pt-specific activity.

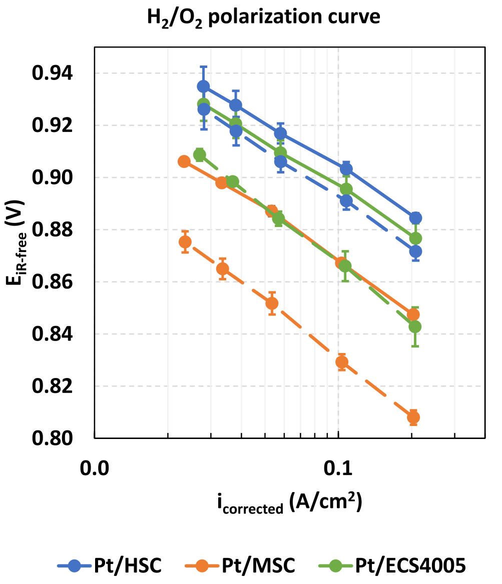

Figure 7. H_2/O_2 polarization curves of the various catalysts measured at 80 °C, 100% RH, 150 kPa_{abs}, and at cathode Pt loading of 0.1 mg/cm^2. Solid lines are at BOL, and dashed lines are at EOT after 30,000 voltage cycles.

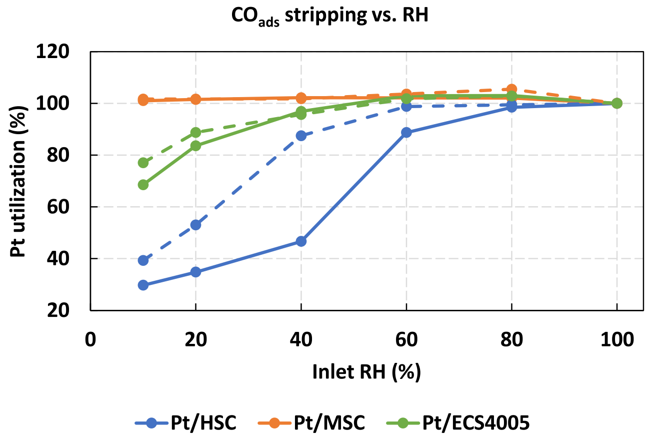

Figure 8. CO_{ads} stripping surface area measured as a function of the inlet RH in an MEA at 80 °C and 0.1 mg_{Pt}/cm^2. Solid lines are at BOL, and dashed lines are at EOT after 30,000 voltage cycles.

region of the three catalysts at BOL and EOT. The mass activity of the catalyst and the performance in the O_2 polarization curve is merely a reflection of Pt poisoning by the PFSA ionomer in the catalyst layer.[9,10] It is known that the sulfonic acid side chain groups and the $-CF_2-$, $-CF_3-$, and ether functional groups of the PFSA ionomer adsorb on the catalyst surface and act as poison for ORR.[42−45] HSC being a more porous carbon support hosts a large majority of the Pt nanoparticles in the internal surface of the carbon away from direct contact with the ionomer and hence enables a higher ORR activity of 0.61 A/mg_{Pt}. In contrast, MSC carbon, being a very solid material, hosts most of the Pt on the external surface of the carbon in direct contact with the PFSA ionomer and hence leads to a lower mass activity of only 0.13 A/mg_{Pt}. ECS4005 has more accessible mesopores of ∼10 nm to disperse Pt nanoparticles away from the ionomer and hence leads to a mass activity of 0.49 A/mg_{Pt}, which indicates significantly better mass activity than Pt/MSC and modestly lower than the Pt/HSC catalyst. Mass activity does degrade more for Pt/ECS4005 (by 63%) and Pt/MSC (69%) compared to Pt/HSC (only 38%), as this is symptomatic of solid carbons with an ordered, graphitic structure (vide infra).[8,25,40] The trend in the O_2 polarization curve of the three catalysts simply reflects the mass activity trends and follows the order Pt/HSC > Pt/ECS4005 > Pt/MSC. The specific activity of the three catalysts increases from 820 to 1124 $\mu A/cm^2$ for Pt/HSC, 212 to 249 $\mu A/cm^2$ for Pt/MSC, and 710 to 777 $\mu A/cm^2$ for Pt/ECS4005. This finding is at

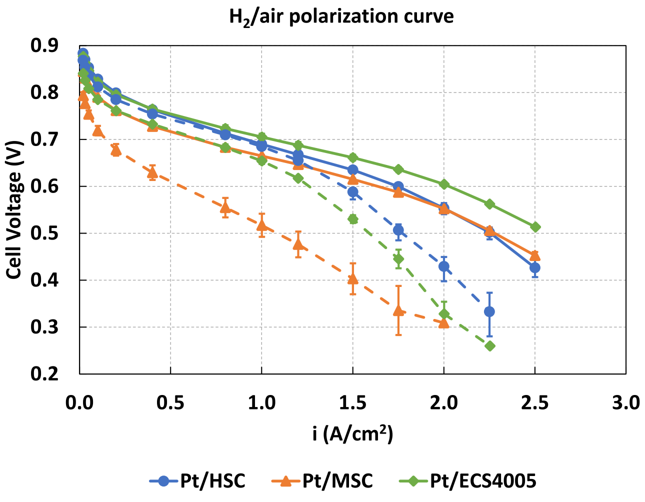

Figure 9. H_2/air polarization curves measured at 80 °C, 100% RH, 150 kPa$_{abs}$, a high stoic of 20, and 0.1 mg$_{Pt}$/cm^2 cathode of the three catalysts. Solid lines are at BOL, and dashed lines are at EOT after 30,000 voltage cycles.

least partly due to the decrease in ECSA of the catalyst and the increase in particle size of Pt, as discussed later in the article.[25,46]

The location distribution of Pt with respect to the carbon support structure can be diagnosed by performing electrochemical CO$_{ads}$ stripping as a function of RH of the catalyst layer, as shown in Figure 8.[47,48] The electrochemical oxidation of CO$_{ads}$ is reliant on water according to the equation Pt-CO$_{ads}$ + H_2O → Pt + CO_2 + 2H$^+$ + 2e$^-$ and hence is dependent on the RH of operation. Under a dry condition of 10% RH, Pt nanoparticles present inside the micro/mesopores of the carbon particles are not accessed. Hence, the dry accessibility represents the fraction of Pt present on the external surface of the carbon in direct contact with the ionomer and equates to ∼30, ∼69, and ∼100% at 10% RH for Pt/HSC, Pt/ECS4005, and Pt/MSC catalysts. This represents Pt that is directly in contact and poisoned by the ionomer. The dry Pt accessibility is also inversely related to the mass activity of the catalyst as this represents the fraction of Pt poisoned by an ionomer.[9,10] As the inlet RH is increased, more Pt that is inside the pores is accessed in the case of Pt/HSC and Pt/ECS4005. Pt/MSC, being a solid carbon, hosts all of the Pt on its external surface and does not show any dependence on RH. After AST, Pt/HSC shows more accessibility in Pt due to either (i) dissolution and redeposition of Pt from the internal surface to the external surface of the carbon support and/or (ii) widening of the carbon micro/mesopores due to corrosion leading to more accessibility of Pt.[7,46] Pt/ECS4005 shows a marginal rise in Pt utilization under dry conditions while Pt/MSC remains unchanged.

Figure 9 shows the differential cell (5 cm^2) H_2/air polarization curve measured with 0.1 mg$_{Pt}$/cm^2 on the cathode at 80 °C, 100% RH, 150 kPa$_{abs}$, and a reactant stoic of 20 at BOL and EOT. At BOL, Pt/ECS4005 shows similar cell voltages in the low current density region (<0.4 A/cm^2) and ∼90 mV higher at 2.5 A/cm^2 compared to Pt/HSC. However, at EOT, Pt/ECS4005 does tend to degrade more in cell voltage by ∼25 mV at 0.2 A/cm^2 and by ∼50 mV at 2.0 A/cm^2 than the Pt/HSC catalyst. Pt/MSC is much lower in cell voltage at the BOL and significantly inferior at the EOT compared to both Pt/HSC and Pt/ECS4005. At EOT, the

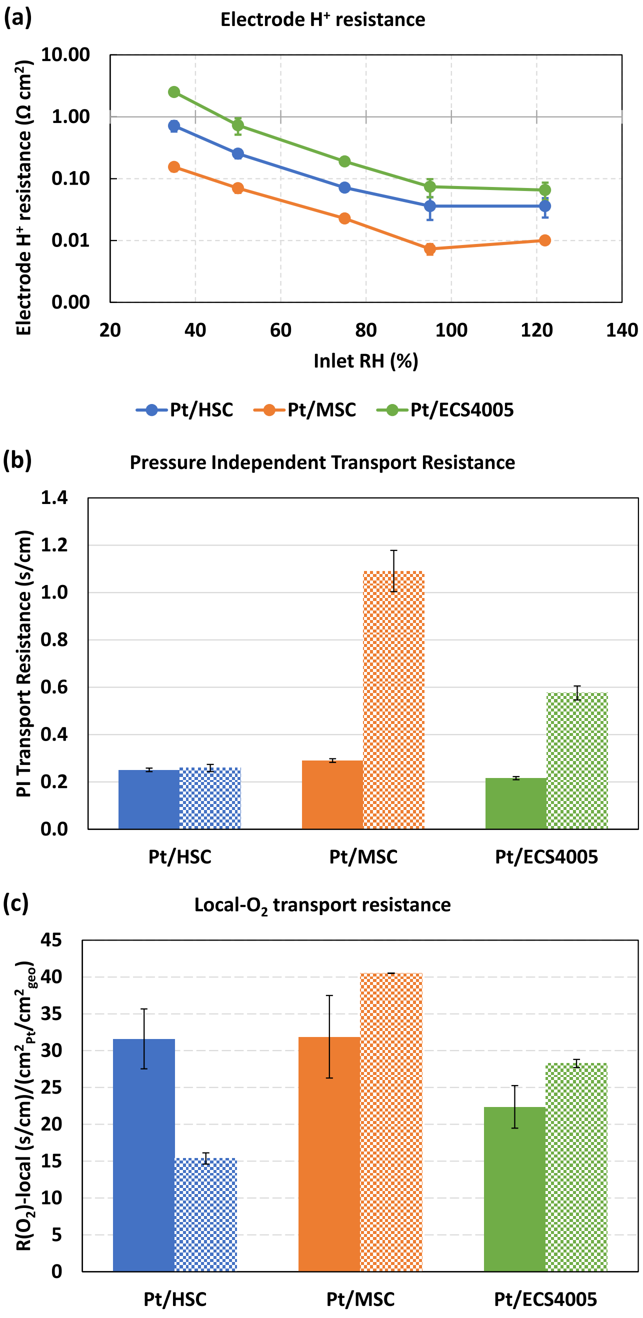

Figure 10. (a) Electrode H$^+$ transport resistance measured from electrochemical impedance spectroscopy measured at anode/cathode flows of H_2/N_2 at 80 °C as a function of RH. (b) Pressure-independent transport resistance and (c) R(O_2)-local obtained by normalizing pressure-independent transport resistance by the roughness factor for each of the three catalysts: closed bars are at BOL and hashed bars are at EOT after 30,000 voltage cycles.

ranking of H_2/air polarization performance is of the order Pt/HSC > Pt/ECS4005 ≫ Pt/MSC. Pt/ECS4005 does tend to lose more cell voltage in the high-current density region, and this is largely related to the ECSA losses, as discussed in Figure 2a. The high-current density performance is directly related to the available Pt surface area.[49] The graphitized, well-ordered nature of ECS4005 does enable the coarsening of Pt and ECSA losses and hence cell voltage losses in the high-current density region as well.

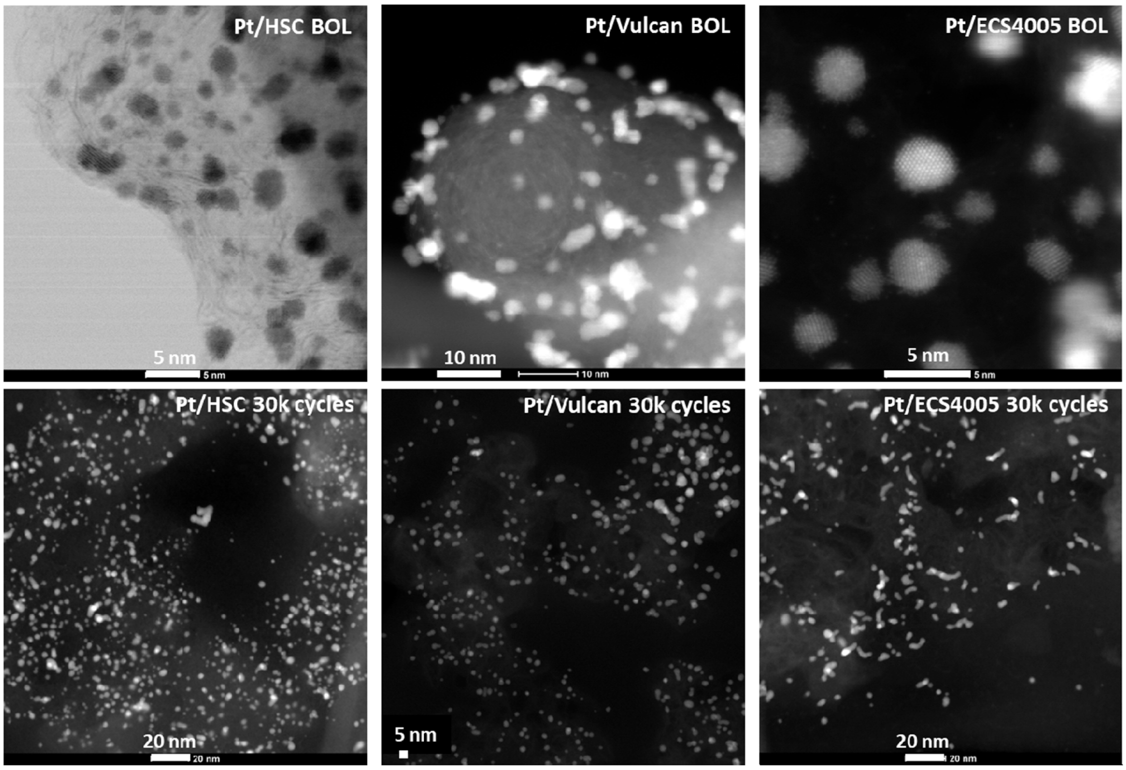

Figure 11. Representative BF/HAADF-STEM images of the three catalysts at BOL and EOT after 30,000 voltage cycles.

Cathode proton transport resistance measured as a function of RH using EIS by flowing anode/cathode gases of H_2/N_2 at 80 °C is shown in Figure 10a.[50] The H^+ transport resistance of the catalyst layer is typically dependent on the macropore surface area of the carbon support.[9] The ionomer is typically dispersed on the macroporous surface area of the carbon; the higher the macropore area, the more surface there is for ionomer dispersion. Hence, Pt/HSC has a higher H^+ transport resistance as its higher macropore surface area causes a given amount of ionomer to be dispersed more thinly on the surface with less connectivity. Pt/MSC yields a lower H^+ transport resistance as its lower macropore surface area causes a more homogeneous and thicker ionomer layer to be dispersed.[9] Pt/ECS4005 has a lower macropore surface area but a higher H^+ transport resistance. Given the ordered, graphitic nature of the ECS4005 carbon support, we hypothesize that it has fewer oxygen functional groups and is more hydrophobic such that ionomer distribution is very heterogeneous and discontinuous on its surface. Further, the ECS4005 carbon features larger primary particle sizes with a higher internal surface area and less accessible macropore surface for ionomer distribution. This likely leads to a higher H^+ transport resistance for the Pt/ECS4005 catalyst.[9,11,24,41]

Figure 10b shows the pressure-independent O_2 transport resistance measured using the O_2-limiting current density experiments, and Figure 10c shows the $R(O_2)$-local obtained by normalizing the pressure-independent transport resistance by the measured roughness factor.[34] Pressure-independent transport resistance corresponds to the O_2 diffusion in the ionomer layer dispersed in the cathode and the Knudsen diffusion resistance in the smaller pores of the catalyst layer.[49] $R(O_2)$-local corresponds to the Pt ECSA-normalized O_2 diffusion resistance at or near the Pt surface. All of the catalysts measured a pressure-independent transport resistance of ~0.25 S/cm at BOL. After normalizing by the BOL ECSA, Pt/ECS4005 shows a lower $R(O_2)$-local of ~22 S/cm compared to ~31 for Pt/HSC and Pt/MSC catalysts. This suggests better Pt accessibility and lower local-O_2 diffusion resistance for the Pt/ECS4005 catalyst due to its mesopore structure. After the AST durability protocol, Pt/MSC and Pt/ECS4005 show an increase in EOT pressure-independent transport resistance. Pressure-independent transport resistance is inversely proportional to the roughness factor or the ECSA of the catalyst and increases at very low ECSA values.[51] The increase in pressure-independent transport resistance at EOT for Pt/MSC and Pt/ECS4005 reflects the lower ECSA values of ~10 and ~21 m^2/g and the poor accessibility of these catalysts at a lower Pt roughness factor. Pt/HSC shows a lower $R(O_2)$-local at EOT, possibly due to some of the internal Pt nanoparticles dissolving and redepositing on the external surface of the carbon support and therefore becoming more accessible by O_2, which is in good agreement with the results from CO_{ads} stripping results above. The $R(O_2)$-local of Pt/ECS4005 at EOT increases as Pt nanoparticles rearrange the carbon support surface but is significantly lower than the baseline solid carbon such as Pt/MSC at EOT.

Figure 11 shows representative STEM images, and Figure 12 shows the particle size distribution (PSD) and aspect ratios of the three catalysts at BOL and EOT. At BOL, Pt/HSC and Pt/ECS4005 appear well dispersed with ~2 nm-sized Pt nanoparticles on the carbon support. Pt/MSC appears to be aggregated on the carbon support with multiple nanoparticles fused together and a slightly elevated average particle size of 3 nm. At EOT, Pt/HSC has grown in particle size to ~3 to 3.5 nm in average size but has largely maintained its spherical shape with an aspect ratio close to 1.2 at EOT.[25] Pt/MSC has grown in average particle size to almost 4 nm with a mix of spherical and elongated particles.[8,25,40] Pt/ECS4005 shows an

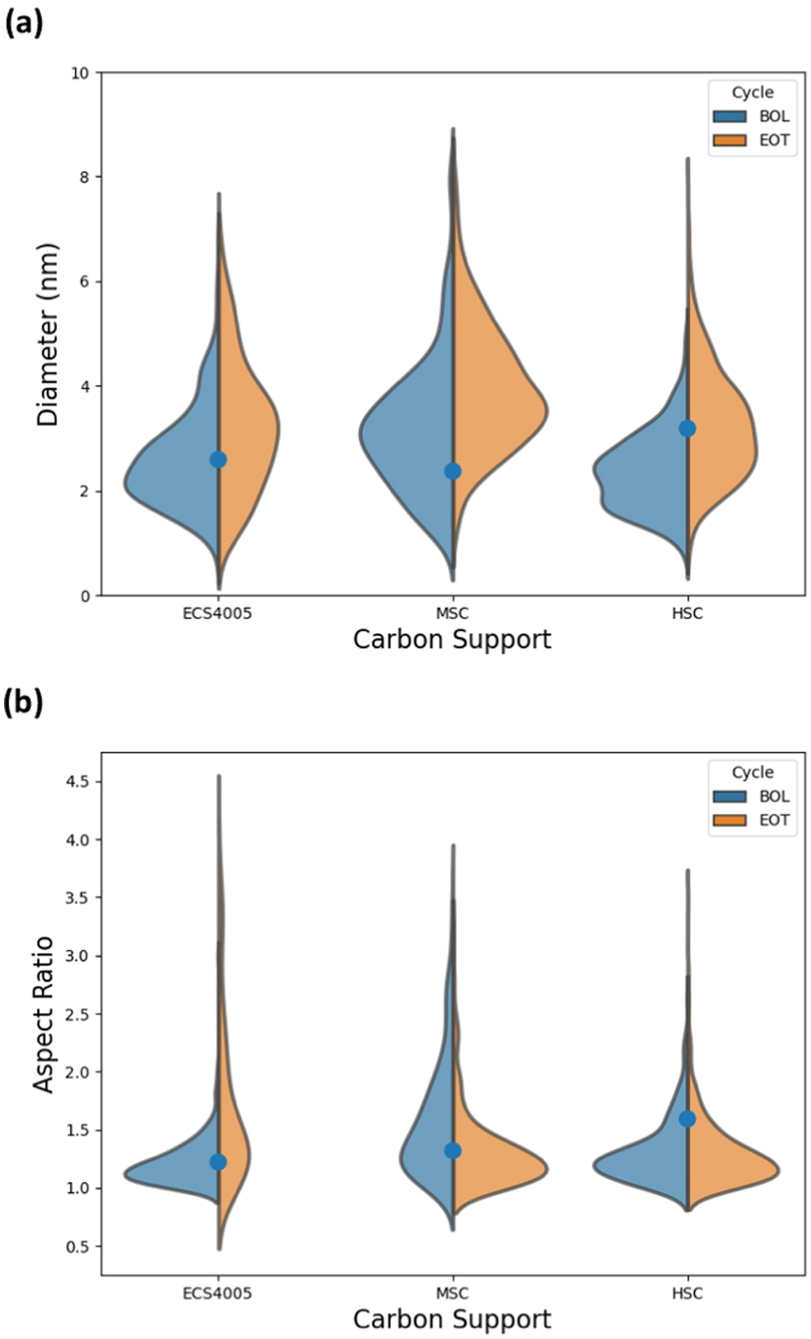

Figure 12. Violin-plot showing (a) the particle size distribution in diameter and (b) the aspect ratio of the catalysts at BOL and EOT after 30,000 voltage cycles, measured from STEM images.

interesting particle size distribution and features elongated particles on the carbon support. It shows an average particle size growth of ∼3.5−4 nm and a higher aspect ratio of 1.4 with a significantly long tail. ECS4005 carbon is a highly graphitized material with well-ordered crystalline planes that enable Pt nanoparticles to slide and migrate on the surface of the carbon support along a specific direction. This leads to the formation of elongated particles with a slight increase in the aspect ratio of the particles.[8,25,40] Pt/ECS4005 represents a significant improvement over the conventional Pt/MSC catalyst with significantly better initial performance and durability; the graphitized and well-ordered ECS4005 carbon surface still presents a durability issue for Pt aggregation. This highlights a challenge in obtaining better catalyst durability with a higher level of graphitization while maintaining a sufficient level of Pt-carbon interaction to anchor the particles.

4. CONCLUSIONS

We have developed a graphitized, mesoporous carbon support (ECS4005) for the deposition of Pt nanoparticles for use in fuel cell cathode applications. ECS4005 features open, accessible mesopores with a size of ∼10 nm for Pt dispersion and 40−80 nm pores for reactant transport. ECS4005 also features high graphitization and well-ordered crystal planes. The favorable features of Pt/ECS4005 enable significantly improved mass activity via mitigation of sulfonate poisoning compared to conventional solid furnace black material such as Vulcan XC-72R, while its accessibility is improved versus Pt/

HSC. BOL H_2/air polarization performance of Pt/ECS4005 in fuel cell MEAs is significantly due to the high mass activity and the open, mesoporous structure that enables improved O_2 mass transport resistance. The durability of the Pt/ECS4005 catalyst is significantly better than Pt/MSC, which is a baseline catalyst for Pt on a solid carbon support. However, the Pt/ECS4005 durability is moderately lower than Pt/HSC, and this result is attributed largely to the graphitized, ordered carbon structure that enables Pt to migrate and coalesce, which leads to the formation of elongated nanoparticles. The lower EOT surface area of Pt/ECS4005 compared to that of the Pt/HSC catalyst causes more than expected high-current density performance losses. Further, the larger primary particle sizes of ECS4005 carbon, with a higher internal surface area, which could be a result of the templated synthesis process, could be accelerating the Pt coarsening process, leading to durability drawbacks. However, the EOT cell voltage of Pt/ECS4005 is significantly better than that of the Pt/MSC catalyst. The development of ECS4005 represents a major step in the direction of a graphitized, mesoporous carbon for fuel cell applications with properties and electrochemical performance significantly better than those of a conventional solid carbon such as Vulcan XC-72R.

■ AUTHOR INFORMATION

Corresponding Author

Nagappan Ramaswamy − *Global Fuel Cell Business, General Motors Company, Pontiac, Michigan 48340, United States;* orcid.org/0000-0002-3430-2758; Email: nagappan.ramaswamy@gm.com

Authors

Barr Zulevi − *Pajarito Powder, Albuquerque, New Mexico 87109, United States;* Present Address: Electric Hydrogen, 3 Strathmore Rd, Natick, Massachusetts 01760, United States

Geoff McCool − *Pajarito Powder, Albuquerque, New Mexico 87109, United States*

Zixiao Shi − *School of Applied and Engineering Physics, Cornell University, Ithaca, New York 14853, United States*

Aldo Chavez − *School of Applied and Engineering Physics, Cornell University, Ithaca, New York 14853, United States*

David A. Muller − *School of Applied and Engineering Physics, Cornell University, Ithaca, New York 14853, United States; Kavli Institute at Cornell for Nanoscale Science, Ithaca, New York 14853, United States*

Anusorn Kongkanand − *Global Fuel Cell Business, General Motors Company, Pontiac, Michigan 48340, United States*

Swami Kumaraguru − *Global Fuel Cell Business, General Motors Company, Pontiac, Michigan 48340, United States*

Complete contact information is available at:
https://pubs.acs.org/10.1021/acsaenm.3c00354

Author Contributions

N.R. led the project and performed electrochemical measurements and physicochemical characterization. B.Z. led the project at Pajarito Powder LLC, and G.M. synthesized the carbon support and catalyst materials. Z.S. performed HR-TEM measurements and analyzed the results. S.K., A.K., and D.M. supervised the project.

Funding

This work was partially supported by the U.S. Department of Energy, Hydrogen, and Fuel Cell Technologies Office (HFTO) under grant DE-EE0008821. Electron microscopy facility support from the Cornell Center for Materials Research under NSF Grant DMR-1719875 is acknowledged.

Notes

The authors declare no competing financial interest.

■ ACKNOWLEDGMENTS

N.R. would like to acknowledge Kenneth Holt, Cristin Keary, and Kathryn Stevick of G.M. for engineering support.

■ REFERENCES

(1) Cullen, D. A.; Neyerlin, K. C.; Ahluwalia, R. K.; Mukundan, R.; More, K. L.; Borup, R. L.; Weber, A. Z.; Myers, D. J.; Kusoglu, A. New roads and challenges for fuel cells in heavy-duty transportation. *Nat. Energy* **2021**, *6* (5), 462−474.

(2) Papageorgopoulos, D. Fuel Cell Technologies Overview, U.S. Department of energy (DOE) hydrogen program 2022 annual merit review proceedings. 2022; Available from: https://www.hydrogen.energy.gov/pdfs/review22/plenary7_papageorgopoulos_2022_o.pdf.

(3) Wang, C.; Spendelow, J. S. Recent developments in Pt−Co catalysts for proton-exchange membrane fuel cells. *Curr. Opin. Electrochem.* **2021**, *28*, No. 100715.

(4) Strasser, P.; Koh, S.; Anniyev, T.; Greeley, J.; More, K.; Yu, C.; Liu, Z.; Kaya, S.; Nordlund, D.; Ogasawara, H.; Toney, M. F.; Nilsson, A. Lattice-strain control of the activity in dealloyed core−shell fuel cell catalysts. *Nat. Chem.* **2010**, *2* (6), 454−460.

(5) Mukerjee, S.; Srinivasan, S.; Soriaga, M. P.; McBreen, J. Role of Structural and Electronic Properties of Pt and Pt Alloys on Electrocatalysis of Oxygen Reduction: An In Situ XANES and EXAFS Investigation. *J. Electrochem. Soc.* **1995**, *142* (5), 1409.

(6) Antolini, E. Carbon supports for low-temperature fuel cell catalysts. *Appl. Catal., B* **2009**, *88* (1), 1−24.

(7) Macauley, N.; Papadias, D. D.; Fairweather, J.; Spernjak, D.; Langlois, D.; Ahluwalia, R.; More, K. L.; Mukundan, R.; Borup, R. L. Carbon Corrosion in PEM Fuel Cells and the Development of Accelerated Stress Tests. *J. Electrochem. Soc.* **2018**, *165* (6), F3148.

(8) Sneed, B. T.; Cullen, D. A.; Reeves, K. S.; Dyck, O. E.; Langlois, D. A.; Mukundan, R.; Borup, R. L.; More, K. L. 3D Analysis of Fuel Cell Electrocatalyst Degradation on Alternate Carbon Supports. *ACS Appl. Mater. Interfaces* **2017**, *9* (35), 29839−29848.

(9) Ramaswamy, N.; Gu, W.; Ziegelbauer, J. M.; Kumaraguru, S. Carbon Support Microstructure Impact on High Current Density Transport Resistances in PEMFC Cathode. *J. Electrochem. Soc.* **2020**, *167* (6), No. 064515.

(10) Yarlagadda, V.; Carpenter, M. K.; Moylan, T. E.; Kukreja, R. S.; Koestner, R.; Gu, W.; Thompson, L.; Kongkanand, A. Boosting Fuel Cell Performance with Accessible Carbon Mesopores. *ACS Energy Lett.* **2018**, *3* (3), 618−621.

(11) Park, Y.-C.; Tokiwa, H.; Kakinuma, K.; Watanabe, M.; Uchida, M. Effects of carbon supports on Pt distribution, ionomer coverage and cathode performance for polymer electrolyte fuel cells. *J. Power Sources* **2016**, *315*, 179−191.

(12) Ortiz-Herrera, J. C.; Cruz-Martínez, H.; Solorza-Feria, O.; Medina, D. I. Recent progress in carbon nanotubes support materials for Pt-based cathode catalysts in PEM fuel cells. *Int. J. Hydrogen Energy* **2022**, *47* (70), 30213−30224.

(13) Pavko, L.; Gatalo, M.; Finšgar, M.; Ruiz-Zepeda, F.; Ehelebe, K.; Kaiser, P.; Geuß, M.; Đukić, T.; Surca, A. K.; Šala, M.; Bele, M.; Cherevko, S.; Genorio, B.; Hodnik, N.; Gaberšček, M. Graphene-Derived Carbon Support Boosts Proton Exchange Membrane Fuel Cell Catalyst Stability. *ACS Catal.* **2022**, *12* (15), 9540−9548.

(14) Liu, M.; Zhang, R.; Chen, W. Graphene-Supported Nanoelectrocatalysts for Fuel Cells: Synthesis, Properties, and Applications. *Chem. Rev.* **2014**, *114* (10), 5117−5160.

(15) Yarlagadda, V.; Ramaswamy, N.; Kukreja, R. S.; Kumaraguru, S. Ordered mesoporous carbon supported fuel cell cathode catalyst for improved oxygen transport. *J. Power Sources* **2022**, *532*, No. 231349.

(16) Joo, S. H.; Choi, S. J.; Oh, I.; Kwak, J.; Liu, Z.; Terasaki, O.; Ryoo, R. Ordered nanoporous arrays of carbon supporting high dispersions of platinum nanoparticles. *Nature* **2001**, *412* (6843), 169−172.

(17) Kamitaka, Y.; Takeshita, T.; Morimoto, Y. MgO-Templated Mesoporous Carbon as a Catalyst Support for Polymer Electrolyte Fuel Cells. *Catalysts* **2018**, *8* (6), 230.

(18) Dzara, M. J.; Godoy, A. O.; Odgaard, M.; Zulevi, B.; Serov, A.; Jankovic, J.; Pylypenko, S. Physicochemical Properties of ECS Supports and Pt/ECS Catalysts. *ACS Applied Energy Materials* **2021**, *4* (9), 9111−9123.

(19) Zhang, W.; Sherrell, P.; Minett, A. I.; Razal, J. M.; Chen, J. Carbon nanotube architectures as catalyst supports for proton exchange membrane fuel cells. *Energy Environ. Sci.* **2010**, *3* (9), 1286−1293.

(20) Li, Y.; Li, Y.; Zhu, E.; McLouth, T.; Chiu, C.-Y.; Huang, X.; Huang, Y. Stabilization of High-Performance Oxygen Reduction Reaction Pt Electrocatalyst Supported on Reduced Graphene Oxide/Carbon Black Composite. *J. Am. Chem. Soc.* **2012**, *134* (30), 12326−12329.

(21) Islam, M. N.; Mansoor Basha, A. B.; Kollath, V. O.; Soleymani, A. P.; Jankovic, J.; Karan, K. Designing fuel cell catalyst support for superior catalytic activity and low mass-transport resistance. *Nat. Commun.* **2022**, *13* (1), No. 6157.

(22) Ott, S.; Du, F.; Luna, M. L.; Dao, T. A.; Cuenya, B. R.; Orfanidi, A.; Strasser, P. Understanding the Performance Increase of Catalysts Supported on N-Functionalized Carbon in PEMFC Catalyst Layers. *J. Electrochem. Soc.* **2022**, *169* (5), No. 054520.

(23) Ott, S.; Orfanidi, A.; Schmies, H.; Anke, B.; Nong, H. N.; Hübner, J.; Gernert, U.; Gliech, M.; Lerch, M.; Strasser, P. Ionomer distribution control in porous carbon-supported catalyst layers for high-power and low Pt-loaded proton exchange membrane fuel cells. *Nat. Mater.* **2020**, *19* (1), 77−85.

(24) Orfanidi, A.; Madkikar, P.; El-Sayed, H. A.; Harzer, G. S.; Kratky, T.; Gasteiger, H. A. The Key to High Performance Low Pt Loaded Electrodes. *J. Electrochem. Soc.* **2017**, *164* (4), F418.

(25) Padgett, E.; Yarlagadda, V.; Holtz, M. E.; Ko, M.; Levin, B. D. A.; Kukreja, R. S.; Ziegelbauer, J. M.; Andrews, R. N.; Ilavsky, J.; Kongkanand, A.; Muller, D. A. Mitigation of PEM Fuel Cell Catalyst Degradation with Porous Carbon Supports. *J. Electrochem. Soc.* **2019**, *166* (4), F198.

(26) Serov, A.; Atanassov, P. Carbendazim-Based Catalytic Materials. U.S. Patent US9,425,464, 2016.

(27) Serov, A.; Halevi, B.; Robson, M.; Patterson, W.; Artyushkova, K.; Atanassov, P. B. Cathode Catalysts for Fuel Cell Application Derived from Polymer Precursors. U.S. Patent US9,502,719, 2016.

(28) Serov, A.; Atanassov, P. Materials with Atomically Dispersed Chemical Moieties. U.S. Patent US10,619,256, 2020.

(29) Serov, A.; Atanassov, P. B. Non-PGM Catalysts for ORR Based on Charge Transfer Organic Complexes. U.S. Patent US9,722,256, 2017.

(30) Serov, A.; Atanassov, P. B.; Halevi, B.; Short, P. Non-PGM Catalyst for ORR Based on Pyrolysed Poly-complexes. U.S. Patent US9,570,761, 2017.

(31) Kabir, S.; Myers, D. J.; Kariuki, N.; Park, J.; Wang, G.; Baker, A.; Macauley, N.; Mukundan, R.; More, K. L.; Neyerlin, K. C. Elucidating the Dynamic Nature of Fuel Cell Electrodes as a Function of Conditioning: An ex Situ Material Characterization and in Situ Electrochemical Diagnostic Study. *ACS Appl. Mater. Interfaces* **2019**, *11* (48), 45016−45030.

(32) Stariha, S.; Macauley, N.; Sneed, B. T.; Langlois, D.; More, K. L.; Mukundan, R.; Borup, R. L. Recent Advances in Catalyst Accelerated Stress Tests for Polymer Electrolyte Membrane Fuel Cells. *J. Electrochem. Soc.* **2018**, *165* (7), F492.

(33) Makharia, R.; Mathias, M.; Baker, D. Measurement of Catalyst Layer Electrolyte Resistance in PEFCs Using Electrochemical Impedance Spectroscopy. *J. Electrochem. Soc.* **2005**, *152*, A970−A977.

(34) Baker, D. R.; Caulk, D. A.; Neyerlin, K. C.; Murphy, M. W. Measurement of Oxygen Transport Resistance in PEM Fuel Cells by Limiting Current Methods. *J. Electrochem. Soc.* **2009**, *156* (9), B991.

(35) Soboleva, T.; Zhao, X.; Malek, K.; Xie, Z.; Navessin, T.; Holdcroft, S. On the Micro-, Meso-, and Macroporous Structures of Polymer Electrolyte Membrane Fuel Cell Catalyst Layers. *ACS Appl. Mater. Interfaces* **2010**, *2* (2), 375−384.

(36) Lowell, S.; Shields, J. E.; Thomas, M. A.; Thommes, M. *Micropore Analysis, in Characterization of Porous Solids and Powders: Surface Area, Pore Size and Density*; Springer: Dordrecht, Netherlands, 2004; pp 129−156.

(37) Cançado, L. G.; Takai, K.; Enoki, T.; Endo, M.; Kim, Y.; Mizusaki, H.; Jorio, A.; Coelho, L.; Paniago, R.; Pimenta, M. General Equation for the Determination of the Crystallite Size L[a] of Nanographite by Raman Spectroscopy. *Appl. Phys. Lett.* **2006**, *88*, 163106.

(38) Hajizadeh, Z.; Taheri-Ledari, R.; Asl, F. R. *3 - Identification and analytical methods, in Heterogeneous Micro and Nanoscale Composites for the Catalysis of Organic Reactions*; Maleki, A., Ed.; Elsevier, 2022; pp 33−51.

(39) Soboleva, T.; Malek, K.; Xie, Z.; Navessin, T.; Holdcroft, S. PEMFC Catalyst Layers: The Role of Micropores and Mesopores on Water Sorption and Fuel Cell Activity. *ACS Appl. Mater. Interfaces* **2011**, *3* (6), 1827−1837.

(40) Tuaev, X.; Rudi, S.; Strasser, P. The impact of the morphology of the carbon support on the activity and stability of nanoparticle fuel cell catalysts. *Catal. Sci. Technol.* **2016**, *6* (23), 8276−8288.

(41) Iden, H.; Ohma, A. An in situ technique for analyzing ionomer coverage in catalyst layers. *J. Electroanal. Chem.* **2013**, *693*, 34−41.

(42) Jomori, S.; Komatsubara, K.; Nonoyama, N.; Kato, M.; Yoshida, T. An Experimental Study of the Effects of Operational History on Activity Changes in a PEMFC. *J. Electrochem. Soc.* **2013**, *160* (9), F1067.

(43) Kodama, K.; Jinnouchi, R.; Suzuki, T.; Murata, H.; Hatanaka, T.; Morimoto, Y. Increase in adsorptivity of sulfonate anions on Pt (111) surface with drying of ionomer. *Electrochem. Commun.* **2013**, *36*, 26−28.

(44) Subbaraman, R.; Strmcnik, D.; Paulikas, A. P.; Stamenkovic, V. R.; Markovic, N. M. Oxygen reduction reaction at three-phase interfaces. *ChemPhysChem* **2010**, *11* (13), 2825−33.

(45) Kodama, K.; Motobayashi, K.; Shinohara, A.; Hasegawa, N.; Kudo, K.; Jinnouchi, R.; Osawa, M.; Morimoto, Y. Effect of the Side-Chain Structure of Perfluoro-Sulfonic Acid Ionomers on the Oxygen Reduction Reaction on the Surface of Pt. *ACS Catal.* **2018**, *8* (1), 694−700.

(46) Ramaswamy, N.; Kumaraguru, S.; Gu, W.; Kukreja, R. S.; Yu, K.; Groom, D.; Ferreira, P. High-Current Density Durability of Pt/C and PtCo/C Catalysts at Similar Particle Sizes in PEMFCs. *J. Electrochem. Soc.* **2021**, *168* (2), No. 024519.

(47) Shinozaki, K.; Yamada, H.; Morimoto, Y. Relative Humidity Dependence of Pt Utilization in Polymer Electrolyte Fuel Cell Electrodes: Effects of Electrode Thickness, Ionomer-to-Carbon Ratio, Ionomer Equivalent Weight, and Carbon Support. *J. Electrochem. Soc.* **2011**, *158* (5), B467.

(48) Padgett, E.; Andrejevic, N.; Liu, Z.; Kongkanand, A.; Gu, W.; Moriyama, K.; Jiang, Y.; Kumaraguru, S.; Moylan, T. E.; Kukreja, R.; Muller, D. A. Editors' Choice—Connecting Fuel Cell Catalyst Nanostructure and Accessibility Using Quantitative Cryo-STEM Tomography. *J. Electrochem. Soc.* **2018**, *165* (3), F173.

(49) Kongkanand, A.; Mathias, M. F. The Priority and Challenge of High-Power Performance of Low-Platinum Proton-Exchange Membrane Fuel Cells. *J. Phys. Chem. Lett.* **2016**, *7* (7), 1127−1137.

(50) Makharia, R.; Mathias, M. F.; Baker, D. R. Measurement of Catalyst Layer Electrolyte Resistance in PEFCs Using Electrochemical Impedance Spectroscopy. *J. Electrochem. Soc.* **2005**, *152* (5), A970.

(51) Della Bella, R. K. F.; Stühmeier, B. M.; Gasteiger, H. A. Universal Correlation between Cathode Roughness Factor and H2/Air Performance Losses in Voltage Cycling-Based Accelerated Stress Tests. *J. Electrochem. Soc.* **2022**, *169* (4), No. 044528.

https://doi.org/10.1021/acsaenm.3c00354
ACS Appl. Eng. Mater. 2023, 1, 2543−2554